Acta Materialia 259 (2023) 119243

Contents lists available at ScienceDirect

Acta Materialia

journal homepage: www.elsevier.com/locate/actamat

Full length article

Segregation-induced grain-boundary precipitation during early stages of liquid-metal embrittlement of an advanced high-strength steel

Y. Ikeda [a], H.C. Ni [b], A. Chakraborty [c], H. Ghassemi-Armaki [d], J.M. Zuo [b], R. Darvishi Kamachali [a], R. Maaß [a,b,*]

[a] Federal Institute of Materials Research and Testing (BAM), Unter den Eichen 87, 12205 Berlin, Germany
[b] Department of Materials Science and Engineering, University of Illinois at Urbana-Champaign, Urbana, IL 61801, USA
[c] ArcelorMittal Global Research and Development, East Chicago, IN 46312, USA
[d] General Motors Global R&D, Manufacturing Systems Research Laboratory, Warren, MI 48092, USA

ARTICLE INFO

Keywords:
liquid-metal embrittlement
steels
grain boundaries
resistance spot welding

Liquid-metal embrittlement (LME) of galvanized (Zn-coated) advanced high-strength steels is a long-known problem in materials science. Here we reveal the initial microstructural processes underneath the Zn-coating that lead to LME-microcrack initiation in the steel substrate. We track the microstructural evolution during the first tens of milliseconds and find pronounced signatures of Fe-Zn intermetallic precipitation in both ferrite grain boundaries and at internal ferrite-oxide phase boundaries. In concert with novel CALPHAD-integrated density-based thermodynamic modelling, we demonstrate that Zn-rich intermetallic phase-nucleation can occur at markedly low processing temperatures due to a segregation transition. We show that a small Zn-enrichment caused by Zn bulk-diffusion during the initial temperature rise in a joining process is sufficient to induce the segregation transition and subsequent nucleation of Fe-Zn intermetallic grain-boundary phases, which the experiments link to crack initiation sites. These findings direct focus onto LME-controlling microstructural and thermodynamic phenomena at temperatures below the ductility trough and the austenite formation temperature.

1. Introduction

Materials science contributes to energy efficiency via the continued development of novel high-performance structural materials that push the strength-ductility envelope. A prominent example are modern advanced high-strength steels (AHSSs) [1–3]. Over the past decades, these alloys have enabled considerable weight reductions in the automotive sector, thereby decreasing greenhouse emissions. A common dual-phase (DP) AHSS [4] consists of a ferrite (α) -martensite (α') (or bainite) microstructure, whereas more complex AHSSs are high Mn-containing transformation-induced plasticity (TRIP) [5] or twinning-induced plasticity (TWIP) steels [6]. To protect such high-grade and advanced alloys from property degradation by corrosion, zinc (Zn) coatings are often applied through a galvanizing process [7,8]. Whilst protective, a Zn-coating comes with problems – the AHSS substrate becomes susceptible to liquid-metal embrittlement (LME) [9–12].

LME is a long-known structural degradation process, in which a liquid metal penetrates a solid substrate. Classical examples are Al-Ga [13–15] or Ni-Bi [16] binaries, and numerous LME-couples are known for iron (Fe), including Fe-Pb [17,18], Fe-Sn [19], or Fe-Zn [9–12], of which the latter one has gained increasing technological relevance with the advent of galvanized AHSSs. Despite the long history and in-depth studies on LME, the fundamental origins of LME in the Fe-Zn system remain unclear, besides the consensus that a large disparity in melting point [20], some local or far-field driving stress, and the ability of the embrittler to penetrate the solid substrate are the basic prerequisites [9,10,21].

In comparison to other LME couples, the low melting temperature of Zn (approx. 693 K [20]), the very short time scales during which LME occurs in joining of AHSSs (typically $<$ 1s [22]), and the complex microstructure of AHSSs [4-6,23], make direct observations essentially impossible. As a result, much of the existing evidence around LME cracks, grain-boundary (GB) weakening, and microstructural changes remain bound to post-mortem studies, where indeed cracks and observations linked to cracked microstructural environments have been the focus. These include Zn infiltrated cracks [9,10,12,24-36], intermetallic phases inside cracks [25,37-40], or preferred GB paths [27-30,41,42].

* Corresponding author.
E-mail address: robert.maass@bam.de (R. Maaß).

https://doi.org/10.1016/j.actamat.2023.119243
Received 16 May 2023; Received in revised form 8 August 2023; Accepted 9 August 2023
Available online 9 August 2023

Such efforts remain mostly studies addressing the micrometer scale signatures of the cracking phenomenon and elementary distributions from which mechanistic interpretations can be made.

Post-mortem micron-scale observations are valuable from a perspective of the occurred material failure but leave a too large gap to the various proposed models [25,29,32,37-39,41-44] that seek explaining the fundamental origin of the structural degradation mechanism. Given the difficulty in bridging between micron-scale post--cracking LME observations and atomic-scale mechanisms, efforts have been made to optimize controlling processing parameters [33,35,45,46], alloying [26,37,47], or to reduce the severity of LME via coating modifications [48,49]. However, selected studies have recently brought light into the atomic-scale and nano-scale structural modifications during LME of the Fe-Zn couple, targeting two central embrittling scenarios: 1) chemical GB weaking via an electronic binding state change [50], and 2) secondary GB phase nucleation [25], both of which alter the interface energy between grains. The two cases have in common that they require fast Zn transport ahead of the crack tip, which may occur via the Gordon-An model [51] of stress-assisted embrittler transport. Remaining a reasonable model for fast Zn diffusion into uncracked GBs, the first case of chemical interface weakening does not include Fe-Zn intermetallic phase formation prior to cracking. In other words, brittle intermetallic phases are not expected ahead of the crack tip in intact GB environments. They would form via additional liquid Zn infiltration and subsequent alloying with the substrate material after cracking, and a crack should not pass-through intermetallic compounds.

In our previous work [25], compelling evidence was presented that the Γ- (Fe_3Zn_{10}) [52], Γ_1- ($Fe_{22}Zn_{78}$) [53] and δ-phase ($Fe_{13}Zn_{126}$) [52,54] are formed prior to cracking, which constitutes the second scenario mentioned above. In conjunction with such nanoscopic phases present in the uncracked GB network, nano-scale transmission electron diffraction revealed the presence of a heterogeneous strain distribution, suggesting strong local lattice-strains. With these new insights into uncracked but LME-affected GBs, questions arose regarding how isolated intermetallic phases can form far away from the actual crack and if insights into the time-evolution of the uncracked GB network during joining can advance the understanding in how Zn can be transported quickly into the steel substrate.

To this end, Zn-transport into the steel substrate as a function of welding current cycles is tracked during resistance spot welding (RSW). With several interruptions to the RSW process, we aim to temporally resolve the emerging critical phenomena leading to LME. Specifically, a detailed microstructural analysis is conducted at ≈1/5 and ≈5/8 of a weld, which demonstrates i) a change in Zn penetration from initial bulk diffusion in combination with preferred solid-state wetting at α/oxide interfaces to GB diffusion and wetting along martensite-GBs (α', at higher temperatures austenite (γ)), and ii) that initial LME-cracking indeed favors GBs in which high Zn-containing intermetallics form as early as after 1/5 of the full weld. This is remarkable, as the local temperature does not rise beyond approx. 520 K during this early stage of LME. To fundamentally understand this, a novel CALPHAD-integrated thermodynamic approach [55,56] is used to investigate the atomic interaction between Zn and Fe at the GBs. Combined with the experiments, the thermodynamic modelling demonstrates that the GBs are undergoing a segregation transition, which has *significant* consequences for subsequent Zn-rich intermetallic formation. The origin and mechanism of this segregation transition are outlined in detail in a related manuscript [57]. In concert, the thermodynamic calculations and experiments suggest that LME-cracking is emerging very early during the process due to thermodynamically favored interfacial intermetallic formation at low temperatures and a subsequent solid wetting phenomenon during continued heating, both of which weaken the GBs significantly.

2. Experimental and computational details

The investigated AHSS is an industrially produced 1.4 mm thick third-generation galvanized sheet steel containing ~6 wt. % alloying elements combining Si, Mn, Al, Cr, Mo, and B with a tensile strength exceeding 1 GPa, and characteristic temperatures, M_s, A_{c1} and A_{c3} being ~ 473 K, 973 K and 1123 K, respectively. To avoid surface oxide formation due to alloying-element segregation to the steel surface, which is known to impair the Zn-coating adhesion [58], the AHSS was annealed in N_2-5%H_2 atmosphere containing a partial pressure, pO_2, of 2.52×10^{-21} atm. This step promotes internal oxides and binds near-surface alloying elements in the steel. Subsequently, galvanization in a Zn-0.2 wt. % Al (Zn-0.5 at. % Al) bath followed, which produced a GI-coating on top of the steel. The GI-AHSS was resistance spot welded in a three-layer stack assembly, where the top sheet was the GI-AHSS, followed by two 1.5 mm thick sheets of galvanized extra deep drawing steel (EDDS), containing 0.002 wt. % C, 0.08 wt. % Mn, 0.10 wt. % P, 0.005 wt. % S, 0.005 wt. % Si, and 0.017 wt. % Cu (0.009 at. % C, 0.08 at. % Mn, 0.18 at. % P, 0.009 at. % S, 0.010 at. % Si, 0.015 at. % Cu). RSW was carried out using a 75/85kVA Taylor-Winfield RSW instrument with a 6 mm diameter copper electrode, following processing conditions that are used in the automotive sector and that follow the SEP1220-2 guidelines. During RSW, a constant electrode force of 4.5 kN and current of 9.2 kA were applied, as schematically depicted in Fig. 1. The applied welding current is just below expulsion, corresponding to the highest current for achieving a maximum nugget size. During a full weld, we differentiate between an electrode squeeze phase, followed by the weld, after which a hold period and electrode unloading is applied (Fig. 1). For the here investigated samples, the duration of the squeeze and hold time were kept constant, being 1167 ms and 300 ms, respectively. However, as indicated in Fig. 1, samples are produced with different welding durations of 83 ms (5 weld cycles), and 250 ms (15 weld cycles), representing microstructural states of an interrupted weld. In addition, the as-galvanized but unwelded microstructure is investigated as to have a well-defined reference state for the intermediate LME-microstructures. Microstructural details and LME after a complete weld (383 ms) were reported on earlier [25].

Following interrupted welding, cross-sectional samples of the weld were prepared. These were mechanically polished according to standard procedures, ending with a chemo-mechanical colloidal silica (50 nm particle size) polish. Microstructural analysis was done using a LEO Gemini 1530 VP scanning electron microscope (SEM) with a Bruker e$^-$Flash^{HD} electron back scattered diffraction (EBSD) detector. Transmission electron microscopes (TEM), JEOL JEM-2200FS with JEOL EX-24065 JGP EDS detector, as well as FEI Thermis Z, were used for detailed structural investigations. TEM specimens were prepared using FEI Quanta 3D FEG focused ion beam (FIB) equipped with an EDAX AMETEK Octane Elect EDS detector and extracted from the steel both in an in-plane and out-of-plane orientation.

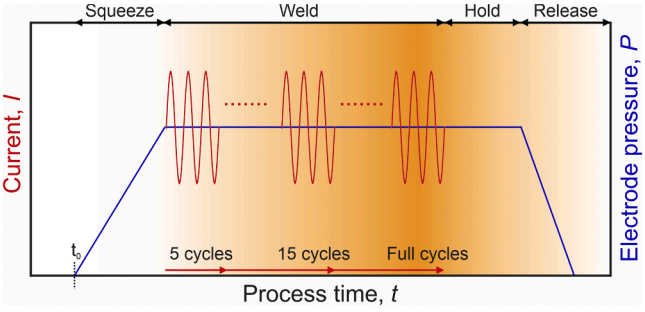

Fig. 1. A schematic showing the RSW sequence and the number of welding cycles. Unwelded, 5 cycles, 15 cycles microstructures are considered, corresponding to 0, 83, and 250 ms of welding time, respectively. The welding time of the full weld corresponds to 383 ms.

The experiments are complemented with finite element method (FEM) simulations using the COMSOL software package [59] to simulate the pressure-temperature profiles at the electrode periphery. Used simulation parameters are summarized in the Table 1. Through the FEM simulations, the temperature history of the investigated microstructures after 5 cycles and 15 cycles can be assessed (see also Fig. 10, Discussion Section).

To further shed light onto observed GB-phenomena, CALPHAD-integrated density-based thermodynamic modeling is performed for studying the segregation and precipitation in an α-GB. While based on the robust CALPHAD approach, the density-based model has been successfully applied when studying GB phenomena in a broad range of materials including steels, Al alloys and high-entropy alloys [56,60-62]. In this model, the thermodynamic properties are expressed as a function of composition and atomic density per unit volume. Central to this approach is that the atomic density, ρ, of the GB is reduced relative to the adjacent bulk material by which the GB free energy is linked to the bulk thermodynamic data [55,63]. For an α-GB in the Fe-Zn binary system, the Gibbs free energy can be described as follows:

$$G^{\alpha}(T,\ \rho,\ x_{Zn}) = x_{Fe}G^{\alpha}_{\mathrm{Fe}}(T,\ \rho) + x_{Zn}G^{\alpha}_{\mathrm{Zn}}(T,\ \rho) + \rho_2 \Delta H^{\alpha}_{\mathrm{Fe,\ Zn}}(T,\ x_{\mathrm{Zn}}) - T\Delta S^{\alpha}_{\mathrm{mix}}(T,\ x_{\mathrm{Zn}}) \quad (1)$$

with

$$G^{\alpha}_{i}(T,\ \rho) = \rho^2 E^{B}_{i} + \rho\left(G^{B}_{i}(T) - E^{B}_{i}\right). \quad (2)$$

Here, E^{B}_{i} and G^{B}_{i} are the potential energy and the Gibbs free energy of a pure substance i, and $\Delta H^{\alpha}_{\mathrm{Fe,\ Zn}}$ and $\Delta S^{\alpha}_{\mathrm{mix}}$ are the mixing-enthalpy and -entropy changes, respectively, which are determined via the Thermo-Calc TCFE11 database [64]. We use the most recent thermodynamic data, but it should be noted that the excess effect of elastic interactions among solute atoms and GBs are neglected here. Current efforts including such effects in the density-based framework [62], and in particular for the Fe-Zn system, are underway. In this study, the value of ρ is set to be 0.9 to generically assess the thermodynamic consequences for a high-angle BCC Fe(α)-GB between two Zn-containing grains. The GB segregation behavior is determined by applying the equal chemical potential condition, and the formation of Γ precipitates at the GB in association with Zn segregation is subsequently studied. Further computational details can be found in Ref. [57].

3. Results

3.1. Microstructure of the as-galvanized sample

In order to quantify the microstructural changes during processing and therefore LME, the as-galvanized unwelded material is examined first. Fig. 2 summarizes the essential features of this as-galvanized state, exhibiting a coarse-grained structure immediately underneath the steel/coating interface (Fig. 2a) as visualized with SEM in backscatter electron (BSE) contrast. EBSD reveals that coarse α grains dominate the near coating region, whereas the matrix consists of α, retained γ, and α' (Fig. 2a and b). Mapped over the area displayed in Fig. 2c, higher concentrations of oxygen as well as Mn, Si, Al were identified with EDS along α-GBs near the coating interface (Figs. 2e-h), indicating the formation of GB-oxides containing Mn, Si, and Al [41,65]. Within the resolution of EDS, no Zn can be detected in the steel or at GBs underneath the coating (Fig. 2d), demonstrating that Zn diffusion into the substrate has not occurred during the galvanization process.

A more detailed microstructural characterization of the near coating region was done using TEM, revealing sub-micron particles as well as GB-precipitates (Fig. 3a). These particles and precipitates are again found to be (Mn, Si, Al)-oxides, as deduced from EDS mapping, of which selected element distributions are depicted in Figs. 3c-e. Similar microstructural heterogeneity in the approximately top 25 µm subsurface region has been reported earlier when focusing on the effects of annealing prior to galvanization [66]. In the remainder of the document, this near surface layer is referred to as the coating substructure. Despite the marked microstructural variation of grain size, phase distribution, and presence of oxides, the as-galvanized state does not reveal any microscopic Zn inside the steel (Fig. 3b). As such, the Zn-coating is predominantly in contact with α and α-GBs.

Table 1
Parameters used in the RSW-FEM simulations

Parameter	Value	Unit
Plate thickness	1.4	mm
Squeeze time	40	ms
Welding time	380	ms
Hold time	300	ms
Off time	500	ms
Welding current	9.2	kA
Frequency	50	Hz
Applied force	4.5	kN
Air temperature	293.15	K
Heat transfer	25	$W{\cdot}m^{-2}{\cdot}K^{-1}$

3.2. Microstructure after 5 cycles

Applying an interrupted weld of 5 cycles (Fig. 1), equivalent to 83 ms processing time, leads to an incomplete weld. Post-welding analysis with SEM shows no indications for any intergranular cracking. However, clear differences in comparison to the as-galvanized steel in the coating substructure of the steel are observed. First, the coating substructure observed in the as-galvanized steel has essentially disappeared at this observation length scale. The original transition from the substructure to the bulk material is indicated with a dashed line in Fig. 4a but cannot anymore be discerned by the former transition to a coarse-grained microstructure in the substructure. Second, Zn has begun to infiltrate the steel substrate, which is demonstrated by SEM-EDS scans in Fig. 4b. This Zn-penetration appears over an approximate distance of 2-3 µm and emerges as a front that moves into the steel. This volumetric transport is much different than the commonly presented highly localized Zn-traces in fully processed Fe-Zn couples [25,26,29,31,38,39,42,44].

More detailed investigations of the substructure after 5 cycles welding are done by BF-STEM and STEM-EDS, summarized in Fig. 5. At this higher resolution, it becomes clear that the coarse-grained ferritic microstructure that initially extended 25 µm into the steel has now reduced to ca. 4 µm from the surface (Fig. 5a). Although the elemental Zn SEM-EDS map shown in Fig. 4b presents a rather homogeneous distribution, STEM-EDS mapping shown in Fig. 5b reveals a much more heterogeneous picture. This discrepancy arises due to the difference in interaction volumes of both used methods. Now, preferential Zn-penetration is seen along α/oxide phase boundaries (Fig. 5c and d) and along α-GBs (Figs. 5e and f). The very diffuse Zn distribution around the α-GBs indicates a solution gradient away from the boundaries but is also convoluted with an image projection. In other words, the GB is clearly detectable via crystallography, whereas the Zn distribution only vaguely marks the GB with the highest Zn concentration of around 50 at. %. A much more distinct Zn-layer is generally observed around the oxides (Figs. 5c and d), where α/oxide interface peak-concentrations of up to 25 at. % are measured, which with increasing distance to the oxide decay to less than 10 at. % (Fig. 5g). In contrast to the α/α-boundaries, the α/oxide-boundaries exhibit a very homogeneous Zn profile around the oxide inclusions. This, and the high Zn concentration near the oxides suggests solid-state wetting [67] at the phase boundaries. In addition to the enhanced Zn interface concentrations, islands of high Zn content are found across the substructure. Using selected-area diffraction (SAD, Figs. 5h and i), they can be identified as Γ-phase grains and they are mostly observed around oxides and at α-GBs. That means, the Fe_3Zn_{10}-intermetallic phase has already formed at this early stage of welding. Yet, LME cracking still remains absent.

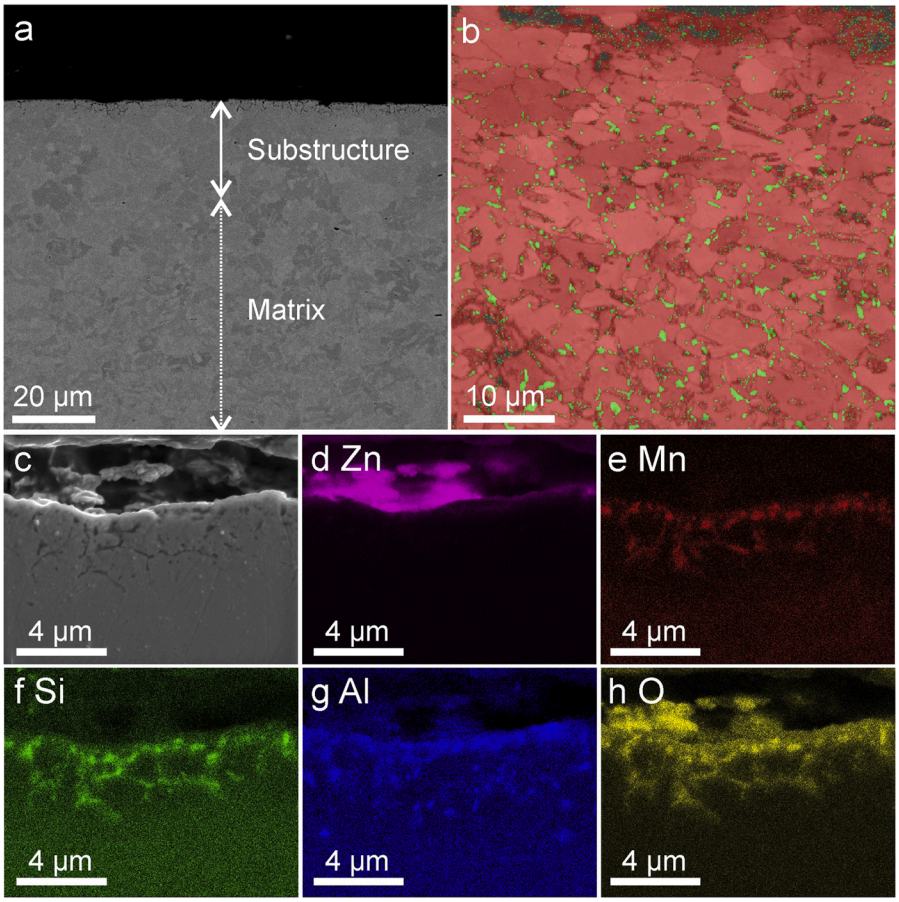

Fig. 2. a) BSE cross-sectional micrograph showing the microstructure of the galvanized steel. The depth of the surface substructure is indicated by the white arrow (approximately 25 ~ 30 microns). b) Phase distribution map obtained by SEM-EBSD showing that the dominant phase is α. The rest of the microstructure consists of α', bainite, and retained γ. Elemental mapping was performed across the region shown in c). d) to h) Elemental maps of Zn, Mn, Si, Al, and oxygen at the steel/coating interface, respectively. The distribution of Mn, Si, Al, and O clearly indicates the formation of GB oxides. Zn diffusion into the substrate is not resolvable.

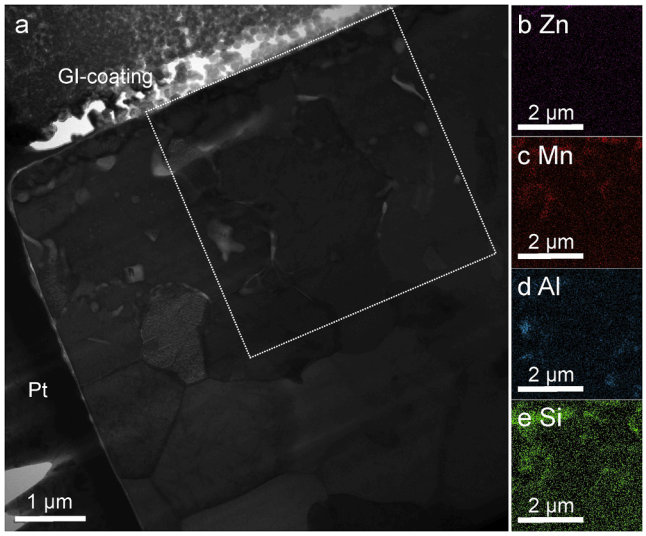

Fig. 3. a) BF-STEM micrograph showing the microstructure of the coating substructure. Brighter regions along the GBs indicate the formation of internal oxides. b) to e) Elemental maps of Zn, Mn, Al, and Si obtained by STEM-EDS. As can be seen, (Mn, Si, Al)-oxides are distributed inside grains as well as along the GBs connecting towards the steel/coating interface.

3.3. Microstructure after 15 cycles

Adding 10 more weld cycles, which amounts to ca. 170 ms additional processing time, yields a dramatically different microstructural picture. Now, several Zn-infiltration paths along GBs can be identified in the electrode periphery. Fig. 6a exemplifies this with a Zn path along GBs that extends ca. 30 μm below the steel/coating interface. The EDS Zn map shown in Fig. 6b corresponds to the indicated dotted box in Fig. 6a and clearly demonstrates how Zn is now present at the GBs instead of within the grains. The typical widths of these Zn traces decrease with distance away from the surface, reducing from a few hundred nm to several 10s of nm. We emphasize that the local Zn concentration highlighted in Fig. 6b does not coincide with any resolvable crack at this observation scale. Along with the numerous Zn traces along GBs, the microstructure changed from still ferritic after 5 cycles to almost exclusively α' after 15 cycles. This means, the steel temperature must have risen above the Ac3 temperature (1123 K), where α transforms into γ that upon cooling results in the martensitic structure seen at room temperature.

TEM observations of the substructure provide a more detailed view of the phase mixture and Zn distribution after 15 weld cycles (Fig. 7a). Now the strong presence of $\boldsymbol{\alpha}'$ can be seen (Fig. 7b), also revealing pockets of retained $\boldsymbol{\alpha}$ that is preferentially located along a crack path that is situated only a few microns away from the sample surface. Such retained polygonal $\boldsymbol{\alpha}$ indicates that the Zn concentration was locally too high and therefore outside of the existence domain for $\boldsymbol{\gamma}$, which has a maximum Zn solubility of ca. 10 at. % [20]. An example of such a Zn-enriched GB is shown in Fig. 7c, showing a strongly heterogeneous chemical distribution. SAD is again used to investigate if the Zn-enrichment is present in the form of elementary pure Zn or if a Fe-Zn intermetallic has formed. The latter is the case, as demonstrated in Figs. 7d and 7e, showing the presence of the $\boldsymbol{\Gamma}$-phase that is discontinuously distributed and follows the chemical heterogeneity seen with EDS. Tracing the infiltration path, $\boldsymbol{\Gamma}$- and $\boldsymbol{\alpha}$-grains can be located alongside with it in surface near regions, whereas further into the substrate $\boldsymbol{\alpha}'$ dominates the microstructure.

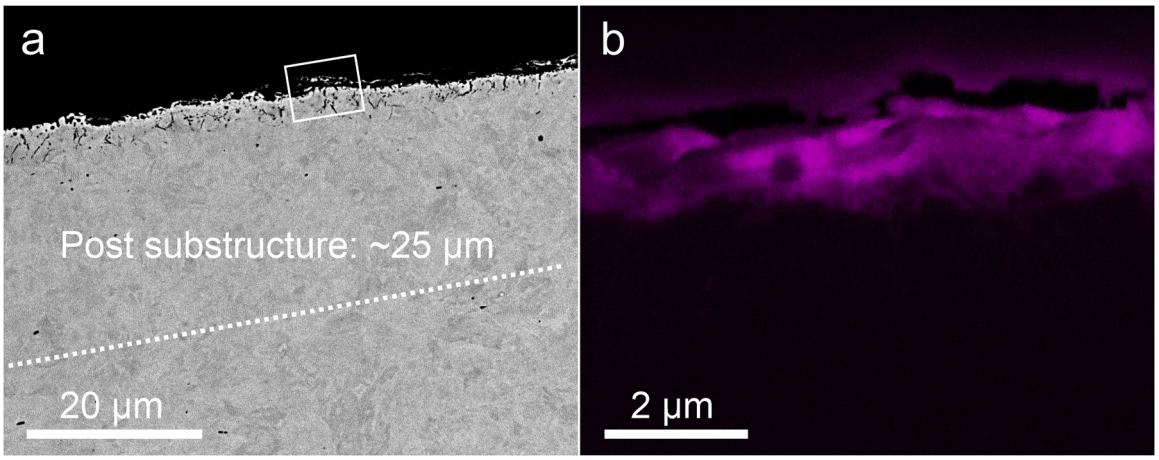

Fig. 4. a) BSE micrograph showing the subsurface microstructure of the 5 cycles sample. The coating substructure, which was extending into the top 25 µm of the unwelded sample, as indicted with the dashed line, is not anymore identifiable. b) EDS elemental mapping of Zn for the surface region indicated in a), clearly revealing Zn diffusion into the AHSS.

In order to shed a more detailed light onto the role of Fe-Zn intermetallic formation after 15 cycles, STEM-EDS and STEM is employed at the tip of a localized Zn-infiltration path along GBs. Fig. 8a displays an overview of such an environment, where the Zn-trace (Fig. 8b) is now confined to $\boldsymbol{\alpha}'$-GBs (prior $\boldsymbol{\gamma}$-GBs). It is important to keep in mind that this is a non-cracked environment and the local TEM-resolved crack discussed in Fig. 7a is located approximately 10-15 µm further away in the direction towards the surface. The several µm long Zn-enriched GB-path becomes discontinuous with varying the infiltration width of several 10s of nm at the root (Fig. 8b) and several nm at its outmost front (Fig. 8d). Figs. 8c and 8d are the corresponding zoomed-in BF-STEM images of the boxes c and d in Fig. 8b, respectively. Along its length going from top to bottom in Fig. 8b, the Zn-content decreases, which is exemplified by a concentration exceeding 40 at. % within box c, whereas ca. 5 at. % can be resolved within box d.

The narrow Zn-trace along the GB in Fig. 8b raises again the question in which form the Zn is present. This was investigated using scanning electron nanobeam diffraction (SEND, also known as 4D-STEM [68]) at the tip of the Zn-infiltration path both within box c and box d in Fig. 8b. Figs. 9a and 9b show the areas enclosed by dashed lines in Fig. 8b and that subsequently were mapped with SEND/4D-STEM. Using this method, spatially resolved diffraction patterns allow reconstructing a detailed grain map. For the indicated sub-area in Fig. 9a the corresponding map is shown in Fig. 9c. Fig. 9d depicts the grain map of the mapped sub-area of Fig. 9b. Enclosed with a dashed line in Fig. 9c, direct mapping of diffraction patterns along the infiltration path demonstrates the presence of the Γ_1-phase. A corresponding diffraction pattern is displayed in Fig. 9f. In contrast to such a spatially extended signature of an intermetallic compound, Fig. 9d only reveals superimposed diffraction patterns for both the Γ-phase and α'. Since the complexity of the local diffraction pattern is high and automated analysis of the 16,000 local diffraction patterns may result in misleading information, we begin with only considering diffraction patterns that have an elevated intensity for diffraction vectors ranging between 3.5 and 4.5 nm^{-1}, being all smaller than those expected for α and α' whose length of the shortest g-vector is approximately 5 nm^{-1}. This yields the intensity map shown in Fig. 9e, indicating a few selected regions with outstandingly high intensities (white areas) that are now considered for further analysis. Choosing those patterns as close as possible to a zone axis allows a clear identification of the Fe_3Zn_{10}-intermetallic or Γ-phase as the GB-phase. A corresponding diffraction pattern is shown in Fig. 9g. We note that this approach does not exhaustively capture all GB-phases, as the g-vector range is limited and since some pattern intensities are simply too low to be properly indexed due to the alignment of the crystal with respect to the viewing direction.

Given the large density difference between α (or α') and Fe_3Zn_{10}, which amounts to approximately 5%, expectations are that the local nucleation of the Γ-phase should be accompanied with lattice strain singularities. The presence of these can be revealed using the SEND/4D-STEM diffraction data via the construction of a relative lattice-strain map, the procedure of which is described elsewhere [25]. Fig. 9h reveals how significant lattice-strain enhancements are present along the Zn-containing GB, with specifically high values coinciding with the locations at which Fig. 9e exhibits intensities for the Γ-phase. This match is not perfect when comparing Figs. 9h and 9e, which is attributed to the fact that not all the Γ-nanograins within the GB align crystallographically with the applied g-vector filter. Furthermore, the thermo-mechanical history of the sample is expected to yield a rather complex internal strain distribution that will be convoluted with the expansion-strain arising from the Γ-phase. Nevertheless, these detailed insights clearly show how the Zn far ahead of the crack tip already promotes the formation of a brittle and lattice-strain generating intermetallic phase in the GB-network early during the process.

4. Discussion

4.1. Intermetallic formation at temperatures below the ductility trough

In view of the outlined and detailed microstructural evolution during LME, it is initially instructive to put the present results into the context of the temperature and mechanical pressure as a function of time. Whilst not directly accessible during the experiments, a good insight into the temperature and stress fields can be gained through FEM simulation using the COMSOL package (see also Methods Section) [59]. Fig. 10 summarizes the effective (von Mises) stress and the temperature as a function of time in the periphery of the weld. The precise location relative to the electrode to which the data in Fig. 10 applies, is indicated with an arrow in the schematic shown in the inset of Fig. 10. Vertically shaded areas extending over the first 83 ms (5 cylces) and 250 ms (15 cycles) cover the process time of the here investigated microstructures. The initial stress peak corresponds to the application of the electrodes onto the weld stack and subsequent stress relaxation due to deformation, and the second stress peak after ca. 120 ms emerges in response to thermal stresses that develop during heating. These are able to relax upon continued heating.

The FEM simulations of the first 83 ms are in good agreement with the observation that Figs. 4 and 5 mostly reveal α. After 250 ms (15 cycles) a temperature somewhat above to the Ac3 temperature is

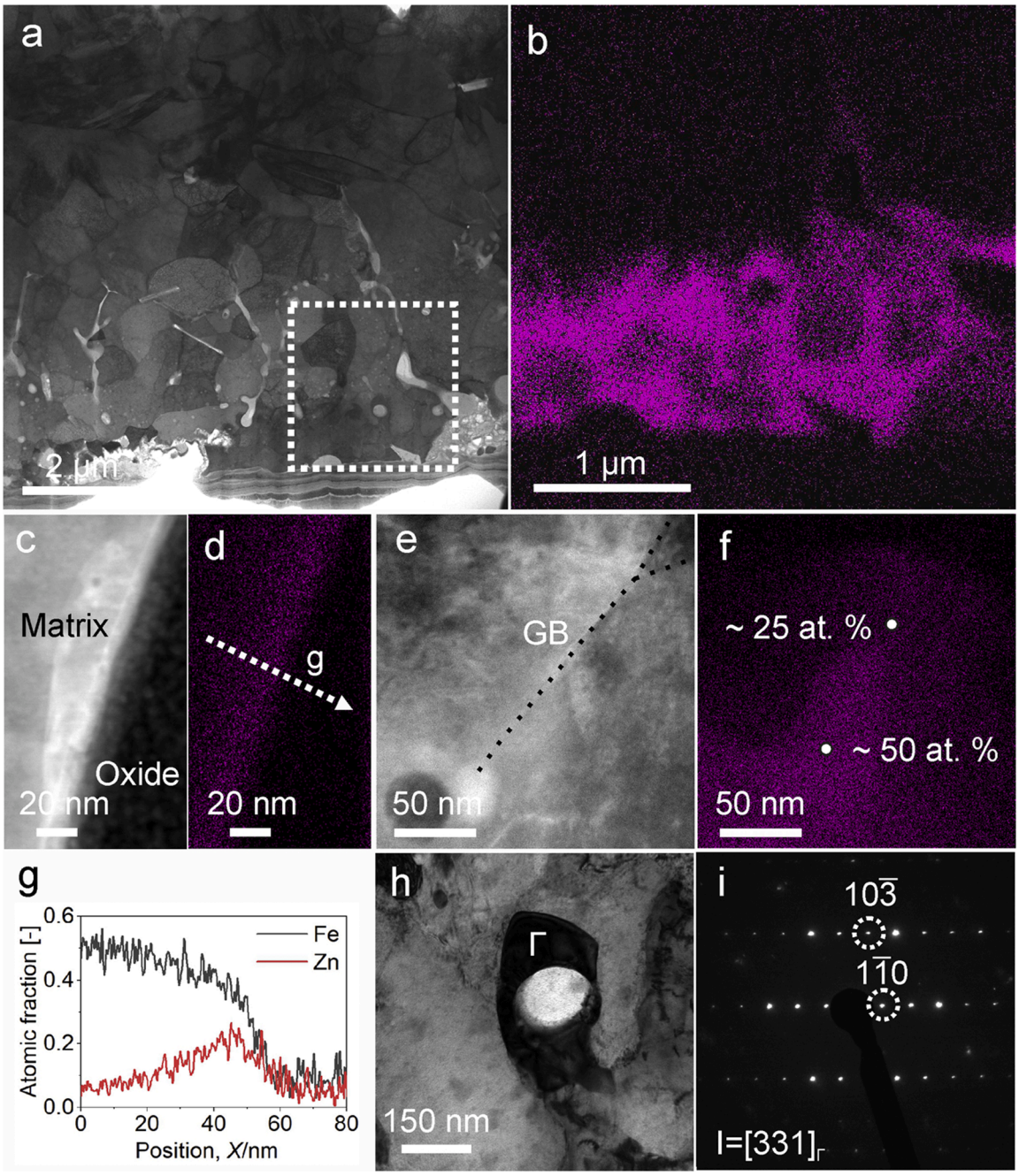

Fig. 5. a) BF-STEM micrograph of the coating substructure of the 5 cycles sample. b) Zn elemental map revealing a heterogeneous distribution of Zn in the area enclosed by a dashed line in a). c) and d) HAADF-STEM micrographs and Zn elemental maps at the **α**/oxide-interface, respectively. e) and f) BF-STEM micrograph and a STEM-EDS map showing the Zn distribution at an **α**-GB. g) Concentration profile across an **α**/oxide interface, which shows a maximum concentration of approximately 25 at. % at the interface. h) BF-TEM micrograph of an Fe-Zn compound formed around a GB oxide, which is identified as the **Γ** − phase by SAD in i).

reached, which is compatible with the corresponding microstructure shown in Figs. 7 and 8 that is dominated by α'. The γ formation-temperature at 1123 K must thus have been passed during the first 15 weld cycles.

Remarkable is, however, that Γ-phase formation and solid wetting of α/oxide-interfaces are already seen after 5 cycles, or 83 ms, which covers the still rising temperature regime in Fig. 10. Even within some error of the FEM-generated temperature profile, it is concluded that the temperature during the first 5 cycles (83 ms) is far below the melting temperature of Zn (693 K) or the ductility trough (973 ~ 1173 K). During these initial 83 ms, volume diffusion into the first few micrometers of the steel substrate occurs with an at STEM-EDS resolution highly heterogeneous Zn distribution, where local concentrations amount (within experimental uncertainty) to 25 at. % and more (Figs. 5d and 5g). Such a high local Zn concentration, at for example an α/oxide-interface, suggest at a solid-state wetting phenomenon [67]. We will see later that thermodynamic calculations indicate how a rather small bulk Zn concentration and a miscibility-gap driven segregation transition can explain the experimental observations after only 83 ms.

Further processing to 250 ms (15 cycles) reveals a dramatic change to an α' dominated microstructure, where all Zn is essentially restricted to the GBs. Microcracking along α' (prior γ) - GBs is observed with TEM, with evidence that crack initiation sites are linked to environments of both the Γ-phase and residual α (Fig. 7). These are close to the substrate

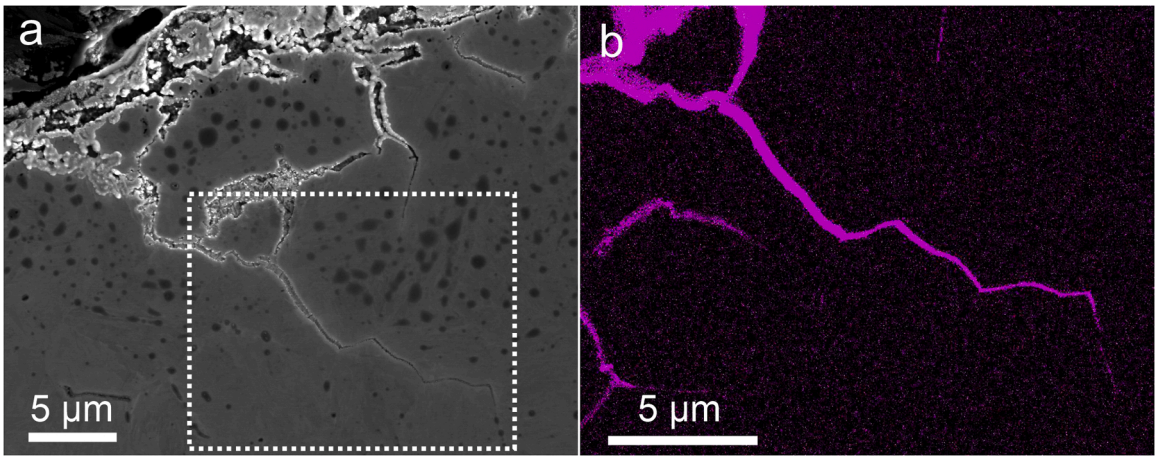

Fig. 6. a) SE image of the 15 cycles sample extracted from the weld periphery region. b) Elemental map of Zn for the area enclosed by a dotted line in a), revealing Zn infiltrated GB-paths that within the resolution of SEM do not reveal decohesion. TEM specimens were extracted at the right most tip of the infiltration path (see Fig. 8).

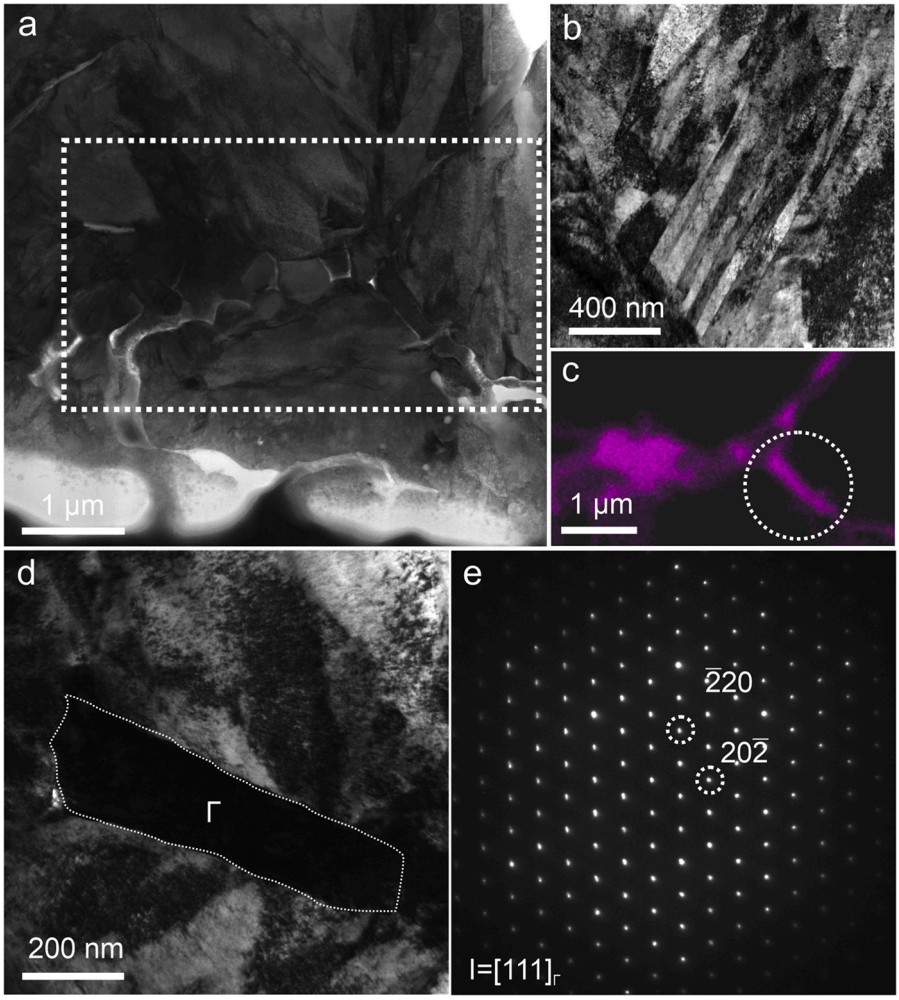

Fig. 7. a) BF-STEM micrograph of the coating substructure of the 15 cycles sample. b) BF-TEM micrograph of the microstructure a few microns away from the Zn infiltration path, showing fine martensitic microstructure. c) Elemental Zn-map recorded within the dotted box in a) that reveals a heterogenous distribution confined to GBs. d) A micrograph in the c) indicated region where Zn accumulation has been observed. e) SAD pattern of the grain indicated in d), revealing the Γ − phase.

surface, which is compatible with the high required Zn-concentrations needed to remain outside the γ phase-domain at high temperatures. Further into the substrate, only α' is observed (Fig. 8).

Tracing the Zn infiltration path along the GBs deeper into the steel substrate reveals a continuously decreasing Zn concentration (Fig. 9). Along the infiltration front, individual Zn containing nm-sized regions

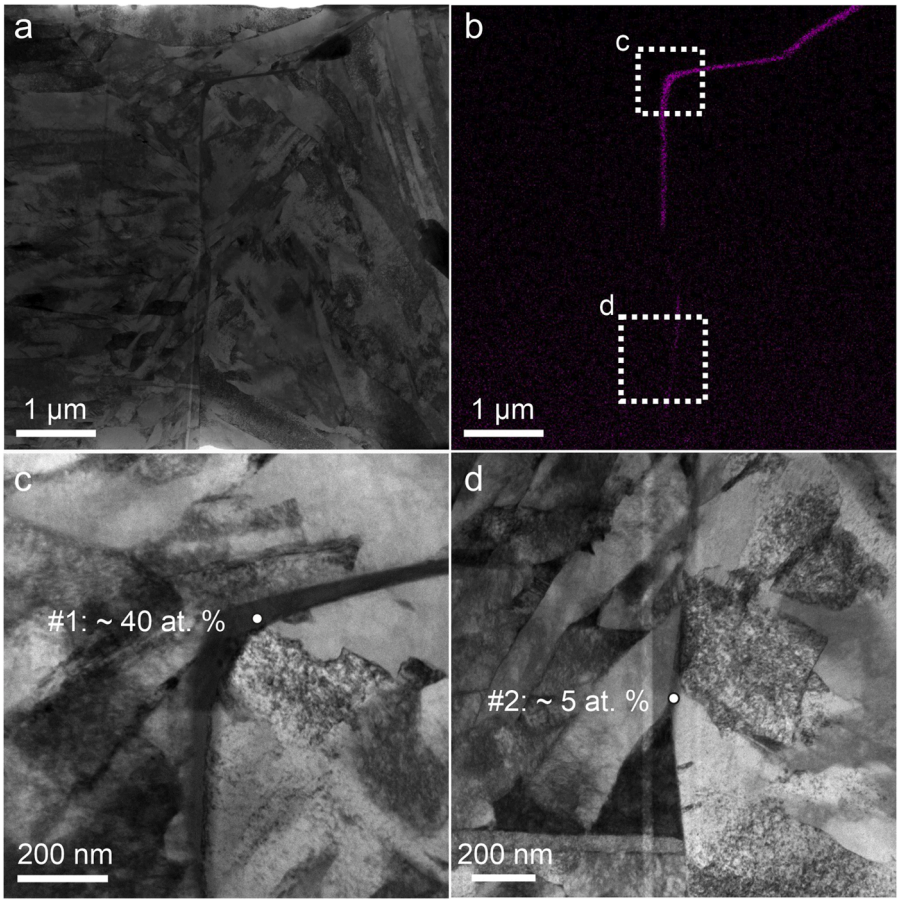

Fig. 8. a) BF-STEM micrograph of the 15 cycles sample at the right-hand tip of the Zn infiltration seen in Fig. 6b. The microstructure is mainly martensitic. b) Elemental map of Zn, showing a Zn distribution along prior γ-GBs. c) and d) BF-STEM images of the infiltration paths that correspond to the dashed boxes in b). The infiltration widths in c) and d) are approximately 50 nm and several nms, respectively.

are identified. SEND and a careful diffraction map analysis demonstrates the presence of nano-scale (~10 nm) Γ-precipitates, around which local lattice strain enhancements are resolvable (Fig. 9). This clearly shows that the Γ-phase is intimately linked to the reaction front between the substrate and the Zn. As soon as Zn is present in either the bulk at the beginning of the process, or in the GB network after the γ-α' transformation, Γ-phase nano-precipitates emerge as a reoccurring microstructural feature. This is surprising, given that local Zn-concentrations can remain well below the required amounts according to the equilibrium Fe-Zn phase diagram [20].

4.2. GB intermetallic-phase formation via a segregation transition

In view of the experimental observations that demonstrate how Zn-rich intermetallic phases, specifically the Γ-phase, form at low temperatures, the question arises how sufficient Zn can locally be supplied? To address this questions, CALPHAD-integrated density-based calculations are conducted, as introduced in the Methods Section. This model enables computing GB thermodynamic free-energy and phase-behavior, as a function of both temperature and alloy composition, as recently demonstrated for selected applications [56,60-62]. Here, this approach is applied to understand the interaction of Zn atoms with the Fe GBs and its influence on the GB precipitation. Before addressing intermetallic phase formation, Zn segregation into α-GBs needs to be understood. The simulations reveal that for only a few atomic percent Zn in the α-grains, adjacent GBs can undergo massive Zn segregation. Corresponding equilibrium segregation isotherms in Fig. 11 show large segregation transitions, i.e., jumps in the segregation isotherms for various temperatures. The giant Zn segregation transition originates from a magnetic miscibility gap in the Fe-Zn system, as is discussed in [57]. The results in Fig. 11 show that for as low as 2 at. % Zn in the bulk alloy, a segregation transition of more than 60 at. % Zn into the GB can occur. The very low amount of Zn required in the solid solution bulk phase emphasizes that the segregation transition is primarily controlled by the thermodynamic driving forces, rather than diffusion of Zn atoms, because even the short time during the early stages of welding is enough to initiate the Zn segregation transition at the GB.

Based on recent investigations that have shown how a GB segregation-transition phenomenon can be accompanied with spinodal-like interfacial phase decomposition [70], also here similar interfacial decomposition with Zn-rich and Zn-poor islands are expected along the α-GB. Note that the spinodal-like interfacial phase decomposition is mainly governed by redistribution of the Zn atoms via short-distance diffusion within the GB plane. As a result of the jump in the segregation isotherms (Fig. 11), interfacial Zn-rich islands with a very high Zn concentration form and thus provide the local requirements for a Γ-phase nucleation at the GBs. This scenario is depicted in Figs. 12a-d. In order to study the possibility of such a segregation-induced GB-precipitation, the energetics of nucleation must be considered. Considering a finite-width of the Zn segregated GB, the energy of nucleation can be described as

$$\Delta G^{\Gamma}_{nucl} = \Delta G \times V + \gamma_{intf} A \tag{3}$$

where $V \approx \frac{\pi}{6}\eta A$ and A are the volume and surface area of the nucleating Γ-precipitate, η is the GB width, $\Delta G = G^{\Gamma} - G^{GB}$ is the driving force for the formation of new Γ phase from the segregated GB, and γ_{intf} is the

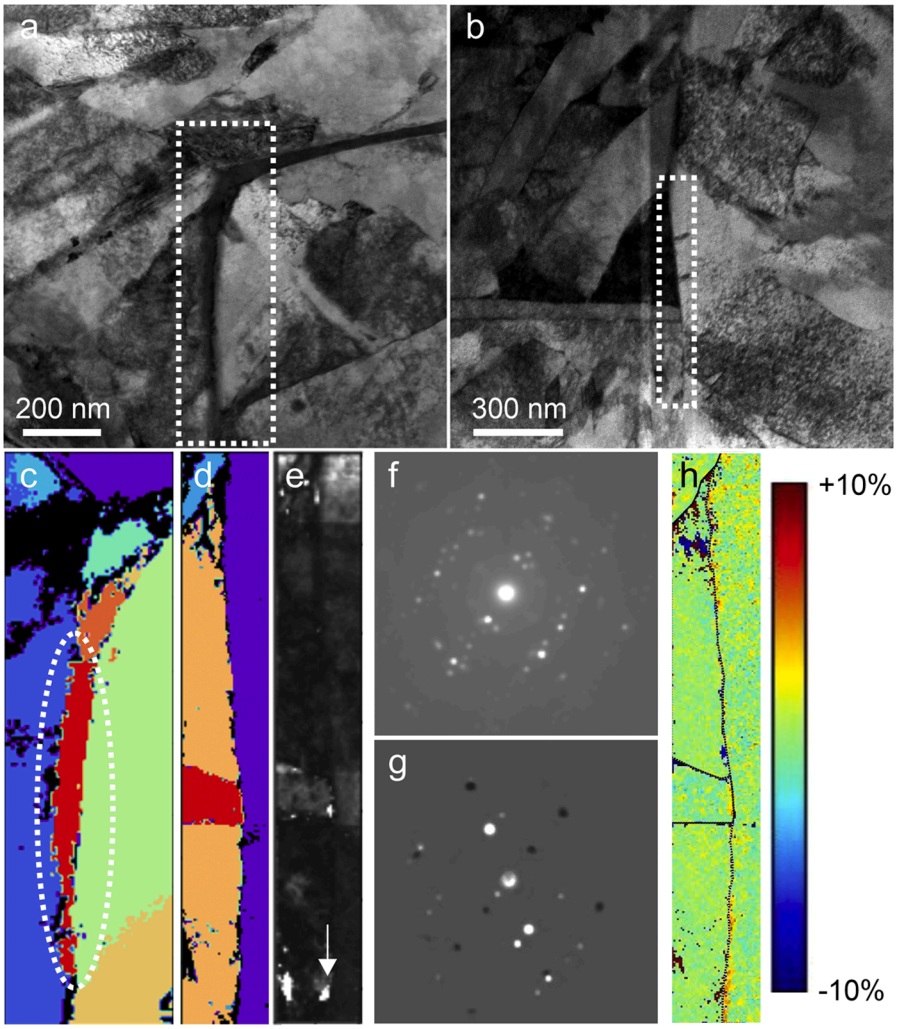

Fig. 9. a) BF-STEM micrograph from the right-hand side of the Zn infiltration path shown in Fig. 6b. The region where SEND is carried out is indicated by the white rectangle, which later corresponds to c). b) BF-STEM micrograph at the front of the Zn infiltration, where the white rectangle marks out the SEND-investigated region that corresponds to d), e), and h). c) and d) pixel classification maps based on the similar features in diffraction patterns of each area indicated in a) and b). e) Intensity map of diffraction spots whose length of g-vector is between 3.5 ~ 4.5 nm^{-1} revealing the presence of a GB phase. f) Integrated diffraction pattern from the region indicated in c), identifying the structure as Γ_1. g) an integrated diffraction pattern from one of the GB phases indicated by the white arrow in e), belonging to the Γ-phase. h) Relative lattice strain map calculated with reference to the literature value of α lattice constant a = 0.2886 nm [69].

energy of the Γ-phase interface. A successful nucleation requires $\Delta G^{\Gamma}_{nucl} < 0$. Even though no information on γ_{intf} is available, the feasibility of the nucleation can still be assessed by studying the driving force, ΔG: Indeed, since $\gamma_{intf} > 0$, the nucleation is only feasible if $\Delta G < 0$. Using the CALPHAD-integrated method, $G^{GB} = G(\rho = 0.9,\ T,\ x_{Zn})$ is computed using Eqs. (1) and (2) and $G^{\Gamma}(T,\ x_{Zn})$ is obtained from the Thermo-Calc TCFE11 database.

Fig. 12e summarizes the obtained free-energy curves for the GB α-phase (G^{GB}) and the Γ-phase (G^{Γ}), across a temperature range from 498 to 873 K. On the same panel, x^{*}_{Zn} values, i.e., the GB compositions corresponding to the jump at the segregation transition-point shown in Fig. 11, and the intersection points between the GB and Γ free energies are depicted by circles and diamonds, respectively, for each temperature.

Assuming the GB segregation-transition compositions, Fig. 12f shows the driving force for precipitation $\Delta G = G(\rho = 0.9,\ T,\ x^{*}_{Zn}) - G^{\Gamma}(T,\ x^{*}_{Zn})$ as a function of temperature. Interestingly, the calculations reveal that with decreasing the temperature, the driving force for the nucleation becomes negative and therefore the Γ phase becomes favorable for temperatures below a critical point at approximately 750 K. This means that the formation of intermetallic Γ-precipitates at the GB is a specific feature in the lower temperature regime. These results rationalize our experimental observations that reveal the interfacial precipitation of Γ-nanoprecipitates in the surface substructure at low temperatures, for which relatively low Zn bulk-concentration seem to be needed. We therefore conclude that the origin of low-temperature Γ-precipitation is the massive segregation transition that increasingly amplifies at lower temperature. Once formed, Γ-precipitates may indeed serve as crack-initiation sites in the subsurface region in which volumetric Zn-transport is seen in the first 83 ms of the microstructural evolution, during which the processing temperature still rises (Fig. 10). This demonstrates that the low-temperature regime during processing becomes critical to understand LME of galvanized high-strength steels.

5. Summary

The fundamental origin of LME in a galvanized advanced high-strength steel was assessed by carefully tracking the microstructural evolution during interrupted welding. Even though industrially viable RSW was used for welding, the findings are generally valid and reveal fundamental new insights into GB-weakening during LME of Fe-Zn, irrespective of the detailed RSW parameters. Focusing on transmission electron microscopy in combination with a novel CALPHAD-integrated thermodynamic approach for studying GB-phenomena, the following conclusions can be made:

- At temperatures well-below the ductility trough, volume diffusion of Zn into the steel occurs, during which high Zn-containing intermetallics form.
- First signatures of local microcracking in the subsurface microstructure are seen in microstructural environments of both retained α and Fe_3Zn_{10} (Γ-phase).

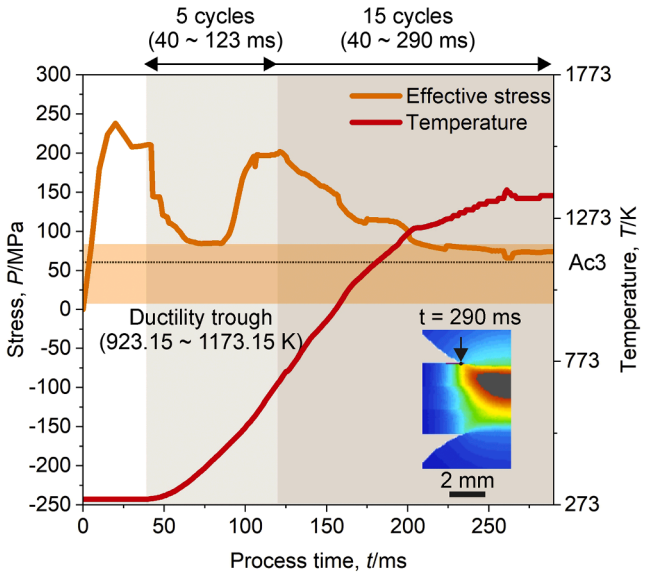

Fig. 10. Stress and temperature profiles derived from COMSOL simulations [59]. The inset shows the temperature distribution after 15 cycles with the arrow indicating the node of the periphery location, from which the data was extracted. This location corresponds to the site of the microstructural observations and welding parameters identical to the experiments were used in the simulations.

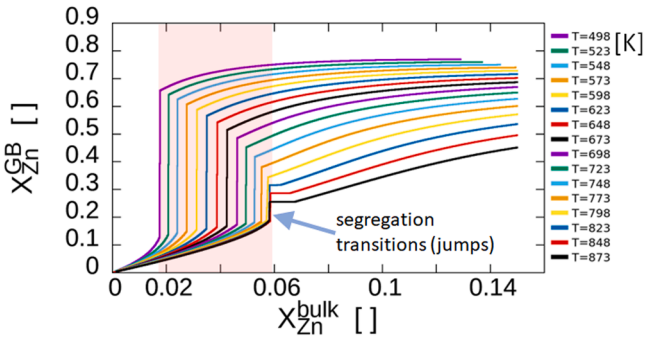

Fig. 11. Zn GB segregation isotherms computed by CALPHAD-integrated density-based modelling. The jumps in the isotherms indicate segregation transitions resulting in a massive increase of the GB Zn content. Temperatures from 498 to 873 K are considered. The segregation increases for lower temperatures. For further details see Ref. [57].

- Once the system passes the austinite-formation temperature and α'-dominates the room-temperature microstructure, Zn is confined to the GB-network, constituting a shift in transport mechanism compared to the low-temperature regime.
- CALPHAD-integrated density-based thermodynamic calculations rationalize how grain-boundary nano-precipitation of Fe_3Zn_{10} can emerge via a significant segregation transition that leads to strong local Zn enrichments in GBs.
- A critical temperature is identified thermodynamically, below which the nucleation of FeZn Γ-phase is favored.

These findings provide strong evidence for that very early GB-phase nucleation at unexpectedly low temperatures is a critical grain-boundary weakening step in LME of galvanized advanced high-strength steels. Once initiated at locations of Γ-nanoprecipitates, crack propagation deeper into the substrate proceeds in conjunction with the γ-α' transformation, at which the Zn transport mechanism changes to be bound to the GBs alone. This later stage of crack propagation has not been tracked here, which also applies to the related Zn transport at the crack tip. However, based on the present observations, we believe that this is a step of secondary importance in the LME damage process. Decohesion and crack initiation seems to be strongly coupled to the early intermetallic nucleation and next steps to strengthen this hypothesis require in-depth DFT calculations that can quantify the changes of GB-energy due to both the presence of Zn and its Fe-Zn intermetallics. Since our conclusion fundamentally relies on the presence of a miscibility gap and a segregation transition [55,57], future work should also focus on its suppression as to mitigate intermetallic GB-phase nucleation.

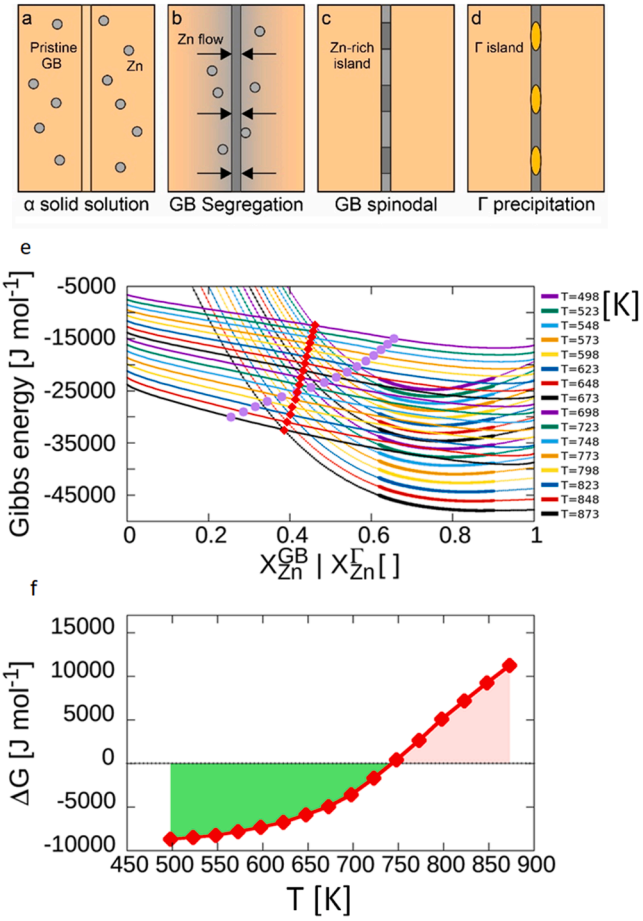

Fig. 12. a) - d) Schematics of the expected GB phase formation sequence. a) Initially, an α solid solution with a GB is considered. b) Zn diffuses from the surrounding matrix towards the GB due to the difference in the chemical potentials. c) a GB segregation-transition occurs and leads to a spinodal-like interfacial pattern with Zn-rich islands once a critical concentration is reached at the GB. d) The Zn-rich islands are favorable nucleation sites for Γ nanoprecipitates. e) Gibbs free energies for the GB and Γ phase for temperatures from 498 to 873 K. The circles mark the segregation transition compositions (x^*_{Zn} values) for the GBs obtained from the segregation isotherms and the diamonds mark the intersection between GB and Γ phase free energies. f) The temperature-dependent driving force for the formation of the Γ phase on Zn-rich islands. Below a critical temperature, the Γ precipitate becomes favorable to form on the segregated GB.

CRediT authorship contribution statement

Y. Ikeda: Formal analysis, Investigation, Writing – original draft, Visualization. **H.C. Ni:** Formal analysis, Investigation. **A. Chakraborty:** Resources, Writing – review & editing. **H. Ghassemi-Armaki:** Resources, Writing – review & editing. **J.M. Zuo:** Supervision. **R. Darvishi Kamachali:** Software, Investigation, Resources, Supervision, Writing –

review & editing. **R. Maaß:** Writing – original draft, Writing – review & editing, Supervision, Conceptualization, Resources, Funding acquisition.

Declaration of Competing Interest

The authors declare that they have no known competing financial interests or personal relationships that could have appeared to influence the work reported in this paper.

Acknowledgements

R.M. is grateful for financial support from ArcelorMittal and the Federal Institute of Materials Research and Testing (BAM). Y.I. gratefully acknowledges the Takenaka Overseas Scholarship Foundation for their kind support of his graduate work, J. Banhart (Technical University Berlin) for institutional support, and C. Prinz for supporting STEM-EDS analysis. R.D.K. acknowledges the support from the German research foundation (DFG) within project DA 1655/3-1 and the Heisenberg program DA 1655/2-1. The authors also thank L. Agudo Jácome, R. Hesse, Q. Hoa-Le and R Saliwan Neumann (all BAM) for the valuable discussions, and Renliang Yuan (UIUC) for TEM data-analysis support. This research was carried out in part at the electron microcopy center at BAM.

References

[1] D. Chatterjee, Behind the Development of Advanced High Strength Steel (AHSS) Including Stainless Steel for Automotive and Structural Applications - An Overview, Materials Science and Metallurgy Engineering 4 (2017) 1–15.
[2] N Baluch, ZM Udin, CS. Abdullah, Advanced High Strength Steel in Auto Industry: an Overview, Engineering, Technology & Applied Science Research 4 (2014) 686–689.
[3] J Zhao, Z. Jiang, Thermomechanical processing of advanced high strength steels, Progress in Materials Science 94 (2018) 174–242.
[4] A Kalhor, M Soleimani, H Mirzadeh, V. Uthaisangsuk, A review of recent progress in mechanical and corrosion properties of dual phase steels, Archives of Civil and Mechanical Engineering (2020) 20.
[5] M Soleimani, A Kalhor, H. Mirzadeh, Transformation-induced plasticity (TRIP) in advanced steels: A review, Materials Science and Engineering: A 795 (2020), 140023.
[6] B.C. De Cooman, OK, K.G. Chin, State-of-the-knowledge on TWIP steel, Materials Science and Technology 28 (2012) 513–527.
[7] AR. Marder, The metallurgy of zinc-coated steel, Progress in Materials Science 45 (2000) 191–271.
[8] J-I Inagaki, M Sakurai, T. Watanabe, Alloying Reactions in Hot Dip Galvanizing and Galvannealing Processes, ISIJ International. 35 (1995) 1388–1393.
[9] SSS Guraja, S Patra, KS Arora, N. Kumar, Liquid Metal Embrittlement (LME) of High-Strength Steels During Spot Welding: A Review, Transactions of the Indian Institute of Metals 75 (2022) 1695–1709.
[10] JE Norkett, MD Dickey, VM. Miller, A Review of Liquid Metal Embrittlement: Cracking Open the Disparate Mechanisms, Metallurgical and Materials Transactions A 52 (2021) 2158–2172.
[11] PJL Fernandes, RE Clegg, DRH. Jones, Failure by liquid metal induced embrittlement, Engineering Failure Analysis 1 (1994) 51–63.
[12] MH Razmpoosh, C DiGiovanni, YN Zhou, E. Biro, Pathway to understand liquid metal embrittlement (LME) in Fe-Zn couple: From fundamentals toward application, Progress in Materials Science (2021) 121.
[13] RGH R.C. Hugo, In-situ TEM observation of aluminium embrittlement by liquid gallium, Scripta Materialia 38 (1998) 523–529.
[14] RGH R.C. Hugo, Gallium penetration of aluminium: in-situ TEM observations at the penetration front, Scripta Materialia 41 (1999) 1341–1346.
[15] RGH R. C. Hugo, The kineitics of gallium penetration into aluminum grain boundaries - *In situ* TEM observations and atomistic models, Acta Materialia 48 (2000) 1949–1957.
[16] K Wolski, N Marié, M. Biscondi, AES quantification of intergranular film thickness in the Ni-Bi system with respect to the liquid metal embrittlement phenomenon, Surface and Interface Analysis 31 (2001) 280–286.
[17] WR Warke, KL Johnson, NN. Breyer, Liquid Metal Embrittlement of Steel by Lead and Lead Alloys, in: JE Draley, JR Weeks (Eds.), Corrosion by Liquid Metals: Proceedings of the Sessions on Corrosion by Liquid Metals of the 1969 Fall Meeting of the Metallurgical Society of AIME, October 13–16, 1969, Philadelphia, Pennsylvania, Springer US, Boston, MA, 1970, pp. 417–439.
[18] T Auger, S Hémery, M Bourcier, C Berdin, M Martin, I. Robertson, Crack path in liquid metal embrittlement: experiments with steels and modeling, Frattura ed Integrità Strutturale 10 (2015) 250–259.
[19] DRHJ R.E. Clegg, Liquid metal embrittlement of tensile specimens of En19 steel by tin, Engineering Failure Analysis 10 (2003) 119–130.
[20] K Han, I Ohnuma, K Okuda, R. Kainuma, Experimental determination of phase diagram in the Zn-Fe binary system, Journal of Alloys and Compounds 737 (2018) 490–504.
[21] Z Ling, M Wang, L. Kong, Liquid Metal Embrittlement of Galvanized Steels During Industrial Processing: A Review, Transactions on Intelligent Welding Manufacturing (2018) 25–42.
[22] DHP Menachem Kimchi, Resistance Spot Welding Fundamentals and Applications for the Automotive Industry, Springer, 2017.
[23] C Kickinger, C Suppan, T Hebesberger, R Schnitzer, C. Hofer, Microstructure and mechanical properties of partially ferritic Q&P steels, Materials Science and Engineering: A 815 (2021), 141296.
[24] D Scheiber, K Prabitz, L Romaner, W. Ecker, The influence of alloying on Zn liquid metal embrittlement in steels, Acta Materialia 195 (2020) 750–760.
[25] Y Ikeda, R Yuan, A Chakraborty, H Ghassemi-Armaki, JM Zuo, R. Maaß, Early stages of liquid-metal embrittlement in an advanced high-strength steel, Materials Today Advances 13 (2022), 100196.
[26] D Bhattacharya, L Cho, J Colburn, D Smith, D Marshall, E van der Aa, et al., Influence of Selected Alloying Variations on Liquid Metal Embrittlement Susceptibility of Quenched and Partitioned Steels, Materials & Design (2022), 111356.
[27] D Bhattacharya, L Cho, E van der Aa, A Pichler, N Pottore, H Ghassemi-Armaki, et al., Influence of the starting microstructure of an advanced high strength steel on the characteristics of Zn-Assisted liquid metal embrittlement, Materials Science and Engineering: A 804 (2021), 140391.
[28] A Ghatei-Kalashami, E Ghassemali, C DiGiovanni, F Goodwin, N. Zhou, Liquid metal embrittlement cracking behavior in iron-zinc (Fe/Zn) couple: Comparison of ferritic and austenitic microstructures, Materials Letters 324 (2022), 132780.
[29] MH Razmpoosh, A Macwan, E Biro, DL Chen, Y Peng, F Goodwin, et al., Liquid metal embrittlement in laser beam welding of Zn-coated 22MnB5 steel, Materials & Design 155 (2018) 375–383.
[30] P Pant, MY Rekha, H Schubert, B Hilpert, LN. Brewer, Liquid metal embrittlement susceptibility of zinc-coated martensitic sheet steels, Materials Science and Engineering: A 863 (2023), 143762.
[31] D Bhattacharya, L Cho, D Marshall, M Walker, E van der Aa, A Pichler, et al., Liquid metal embrittlement susceptibility of two Zn-Coated advanced high strength steels of similar strengths, Materials Science and Engineering: A 823 (2021), 141569.
[32] W Dong, M Lei, H Pan, K Ding, Y. Gao, Role of the internal oxidation layer in the liquid metal embrittlement during the resistance spot welding of the Zn-coated advanced high strength steel, Journal of Materials Research and Technology 21 (2022) 3313–3326.
[33] D Sage, C. Fink, Understanding temperature and dwell time dependence of liquid metal embrittlement in austenitic stainless steel by liquid zinc and copper, Materialia 24 (2022), 101502.
[34] X Wang, Y Xie, Z Liu, Q Sun, X Shen, Q Zhang, et al., Zn-induced liquid metal embrittlement and mechanical properties of advanced high-strength steel with resistance spot weld, Materials Science and Engineering: A 843 (2022), 143088.
[35] J-H Kang, S-H Hong, J Kim, S-J. Kim, Zn-induced liquid metal embrittlement of galvanized high-Mn steel: Strain-rate dependency, Materials Science and Engineering: A 793 (2020), 139996.
[36] D Bhattacharya, L Cho, E van der Aa, H Ghassemi-Armaki, A Pichler, KO Findley, et al., Transgranular cracking in a liquid Zn embrittled high strength steel, Scripta Materialia 175 (2020) 49–54.
[37] S-H Hong, J-H Kang, D Kim, S-J. Kim, Si effect on Zn-assisted liquid metal embrittlement in Zn-coated TWIP steels: Importance of Fe-Zn alloying reaction, Surface and Coatings Technology 393 (2020), 125809.
[38] H Kang, L Cho, C Lee, BC. De Cooman, Zn Penetration in Liquid Metal Embrittled TWIP Steel, Metallurgical and Materials Transactions A 47 (2016) 2885–2905.
[39] CW Lee, WS Choi, L Cho, YR Cho, BC. De Cooman, Liquid-Metal-Induced Embrittlement Related Microcrack Propagation on Zn-coated Press Hardening Steel, ISIJ International 55 (2015) 264–271.
[40] SP Murugan, JB Jeon, C Ji, Y-D Park, Liquid zinc penetration induced intergranular brittle cracking in resistance spot welding of galvannealed advanced high strength steel, Welding in the World 64 (2020) 1957–1969.
[41] AG Kalashami, C DiGiovanni, MH Razmpoosh, F Goodwin, NY. Zhou, The Role of Internal Oxides on the Liquid Metal Embrittlement Cracking During Resistance Spot Welding of the Dual Phase Steel, Metallurgical and Materials Transactions A 51 (2020) 2180–2191.
[42] MH Razmpoosh, A Macwan, F Goodwin, E Biro, Y. Zhou, Role of Random and Coincidence Site Lattice Grain Boundaries in Liquid Metal Embrittlement of Iron (FCC)-Zn Couple, Metallurgical and Materials Transactions A 51 (2020) 3938–3944.
[43] G Jung, IS Woo, DW Suh, S-J. Kim, Liquid Zn assisted embrittlement of advanced high strength steels with different microstructures, Metals and Materials International 22 (2016) 187–195.
[44] CW Lee, DW Fan, IR Sohn, S-J Lee, BC. De Cooman, Liquid-Metal-Induced Embrittlement of Zn-Coated Hot Stamping Steel, Metallurgical and Materials Transactions A 43 (2012) 5122–5127.
[45] C Böhne, G Meschut, M Biegler, M. Rethmeier, Avoidance of liquid metal embrittlement during resistance spot welding by heat input dependent hold time adaption, Science and Technology of Welding and Joining 25 (2020) 617–624.
[46] van der Aa E, Rana R. Optimization of hot forming temperature to minimize liquid metal embrittlement induced cracking in resistance spot welded zinc-coated medium manganese steel. steel research international. 2023.
[47] IO Yilmaz, AY Bilici, H. Aydin, Resistance spot weldability of TBF steel sheets with dissimilar thickness, Metallurgical Research & Technology 117 (2020) 620.

[48] D Kim, SH Hong, JH Kang, YR Im, SJ. Kim, Effect of Zn-Coating Process on Liquid Metal Embrittlement of TRIP Steel, Metals and Materials International 29 (2023) 135–140.
[49] J Zhao, C Ding, G Wu, J. Zhang, Role of aluminum on liquid metal embrittlement susceptibility for Zn–Al–Mg/Sn coated hot-formed steels, Journal of Materials Research and Technology 19 (2022) 747–764.
[50] MH Razmpoosh, B Langelier, E Marzbanrad, HS Zurob, N Zhou, E. Biro, Atomic-scale investigation of liquid-metal-embrittlement crack-path: Revealing mechanism and role of grain boundary chemistry, Acta Materialia 204 (2021), 116519.
[51] HHA Paul Gordon, The mechanisms of crack initiation and crack propagation in metal-induced embrittlement of metals, Metallurgical Transactions A 13A (1982) 457–472.
[52] CHE Belin, RCH. Belin, Synthesis and crystal structure determinations in the Γ and δ Phase domains of the iron–zinc system: Electronic and bonding analysis of Fe13Zn39 and FeZn10, a subtle deviation from the Hume–Rothery standard? Journal of Solid State Chemistry 151 (2000) 85–95.
[53] AS. Koster, Structure of the Cubic Iron-Zinc Phase Fe22Zn78, Acta Cryst B37 (1981) 1905–1907.
[54] HS M.H. Hong, Transmission electron microscopy of the iron-zinc delta 1 intermetallic phase, Scripta Materia 36 (1997) 1423–1429.
[55] R Darvishi Kamachali, A model for grain boundary thermodynamics, RSC Adv 10 (2020) 26728–26741.
[56] L Wang, R Darvishi Kamachali, Density-based grain boundary phase diagrams: Application to Fe-Mn-Cr, Fe-Mn-Ni, Fe-Mn-Co, Fe-Cr-Ni and Fe-Cr-Co alloy systems, Acta Materialia 207 (2021), 116668.
[57] Darvishi Kamachali R, Wallis T, Ikeda Y, Saikia U, Ahmadian A, Liebscher CH, et al. Giant segregation transition as origin of liquid metal embrittlement in the Fe-Zn system. 2023. p. arXiv:2304.13336.
[58] GM Song, T Vystavel, N van der Pers, JTM De Hosson, WG. Sloof, Relation between microstructure and adhesion of hot dip galvanized zinc coatings on dual phase steel, Acta Materialia 60 (2012) 2973–2981.
[59] COMSOL AB S, Sweden. COMSOL Multiphysics® v. 6.1.
[60] LL Li, RD Kamachali, ZM Li, ZF. Zhang, Grain boundary energy effect on grain boundary segregation in an equiatomic high-entropy alloy, Physical Review Materials 4 (2020), 053603.
[61] L Wang, R Darvishi Kamachali, CALPHAD integrated grain boundary co-segregation design: Towards safe high-entropy alloys, Journal of Alloys and Compounds 933 (2023), 167717.
[62] L Wang, R. Darvishi Kamachali, Incorporating elasticity into CALPHAD-informed density-based grain boundary phase diagrams reveals segregation transition in Al-Cu and Al-Cu-Mg alloys, Computational Materials Science 199 (2021), 110717.
[63] R Darvishi Kamachali, A Kwiatkowski da Silva, E McEniry, D Ponge, B Gault, J Neugebauer, et al., Segregation-assisted spinodal and transient spinodal phase separation at grain boundaries, npj Computational Materials 6 (2020) 191.
[64] JO Andersson, T Helander, L Höglund, P Shi, B. Sundman, Thermo-Calc & DICTRA, computational tools for materials science, Calphad 26 (2002) 273–312.
[65] W Mao, RWA Hendrikx, WG. Sloof, Prediction of oxide phases formed upon internal oxidation of advanced high-strength steels, Oxidation of Metals 89 (2017) 531–549.
[66] A Ghatei Kalashami, C DiGiovanni, MH Razmpoosh, F Goodwin, NY Zhou, The effect of silicon content on liquid-metal-embrittlement susceptibility in resistance spot welding of galvanized dual-phase steel, Journal of Manufacturing Processes 57 (2020) 370–379.
[67] GA López, EJ Mittemeijer, BB. Straumal, Grain boundary wetting by a solid phase; microstructural development in a Zn–5 wt% Al alloy, Acta Materialia 52 (2004) 4537–4545.
[68] C. Ophus, Four-dimensional scanning transmission electron microscopy (4D-STEM): From scanning nanodiffraction to ptychography and beyond, Microsc Microanal 25 (2019) 563–582.
[69] R. David, WAB. Wilburn, Hydrostatic compression of iron and related compounds: an overview, American Mineralogis 63 (1978) 591–596.
[70] T Wallis, RD. Kamachali, Grain boundary structural variations amplify segregation transition and stabilize co-existing spinodal interfacial phases, Acta Materialia 242 (2023), 118446.